---

**Article:**
Ferguson, C.G., Christofidou, K.A., Hildyard, E.M. et al. (2020) On the continuous and discontinuous precipitation of the L12 phase in Cu-Ni-Al alloys. Materialia, 13. 100855.

https://doi.org/10.1016/j.mtla.2020.100855

---

# On the continuous and discontinuous precipitation of the $L1_2$ phase in Cu-Ni-Al alloys

Calum G. Ferguson[a], Katerina A. Christofidou[b,*], Emma M. Hildyard[a], Alison S. Wilson[a], Nicholas G. Jones[a], Howard J. Stone[a]

[a]Department of Materials Science and Metallurgy, University of Cambridge, 27 Charles Babbage Road, Cambridge CB3 0FS, UK
[b]Department of Materials Science and Engineering, The University of Sheffield, Sir Robert Hadfield Building, Mappin Street, Sheffield, S1 3JD, UK

∗Corresponding author
Email address: k.christofidou@sheffield.ac.uk (Katerina A. Christofidou)

## Abstract

$L1_2$ precipitate hardened Cu-Ni-Al alloys offer high strength, corrosion resistance and anti-biofouling properties, making them useful in marine engineering applications. Optimisation of their mechanical properties requires a full understanding of their complex precipitate nucleation and coarsening mechanisms. In this work, the microstructural characteristics and hardness of three Cu-Ni-Al alloys with compositions of $Cu_{(95-x)}Ni_xAl_5$ ($x$ = 5, 15, 25 at%) were investigated in the homogenised state and following heat treatments at 700˚C for 1, 10, 100 and 1000 hours. $L1_2$ precipitates were observed in the alloys containing ≥ 15 at% Ni. In these alloys, the $L1_2$ phase was found to precipitate via both continuous and discontinuous routes following all exposures at 700˚C. The coarsening behaviours of the continuous and discontinuous $L1_2$ distributions were characterised and correlated to measurements of hardness and lattice misfit. The alloys containing 15 and 25 at% Ni exhibited peak hardness after 1 h at 700˚C, which corresponded to average particle diameters of 30 nm, respectively. These results were rationalised through calculations of the change in the critical resolved shear stress associated with the transition from weakly to strongly coupled superpartial dislocations. The discontinuous reaction was observed to be led by $L1_2$ phase formation, which extended into the neighbouring grain, ahead of the reorientation front of the matrix.

**Keywords:** Copper alloys, Precipitation kinetics, Discontinuous phenomena, Electron backscatter diffraction

## 1. Introduction

Cupronickel alloys exhibit excellent resistance to aqueous corrosion, hydrogen embrittlement and stress corrosion cracking [1, 2]. The mechanical properties of these alloys may also be enhanced through additions that promote solid solution and/or precipitation strengthening [3, 4]. In addition, these alloys exhibit strong antibiofouling properties due to the high toxicity of Cu to marine life [5]. As a result, they are used extensively in marine engineering, finding applications in ship building, desalination plants, offshore oil platforms and power generation [6, 7].

Traditional cupronickel alloys were developed to exploit the complete miscibility of Cu and Ni that form a solid solution with an A1 structure (Strukterbericht notation) [8]. In order to improve environmental resistance, additions of Al were utilised to form Ni-Al bronzes, which also served to improve the mechanical properties through the formation of precipitates of the $(Ni,Cu)_3Al$ phase, which has the $L1_2$ (Strukterbericht notation) superlattice structure. The ordered $L1_2$ precipitates maintain coherency with the disordered A1 matrix, similar to the structurally analogous γ/γ′ Ni-based superalloys [9]. To date, a number of precipitate hardened cupronickel alloys of this type have been commercially produced for use in structural applications. These include Hiduron® 130, Hiduron® 191 and Marinel®, which have compositions of Cu-14.4Ni-2.7Al-0.8Fe-0.3Mn [4, 3], Cu-14.2Ni-3.9Mn-2.3Al-0.8Fe [10] and Cu-19.6Ni-5.0Mn-4.0Al-1.3Fe-0.5Nb-0.5Cr-0.22Si [11] in at.%, respectively.

In a study of precipitation in Hiduron® 130, two forms of the $L1_2$ phase were observed: small, continuously precipitated intragranular particles and large discontinuously precipitated colonies nucleating from grain boundaries

[12]. Similarly, microstructural investigations of Marinel® identified two distinct precipitating phases: an intragranular $L1_2$ phase and a grain boundary Nb-rich orthorhombic ε phase [11, 13]. In subsequent work, Grylls [14] developed a Bayesian neural network to predict the mechanical properties of precipitation hardened cupronickel alloys as a function of composition. Although, the effect of processing parameters and the associated microstructural changes were not included in their model. More recently, a study of precipitation in Cu-15Ni-xAl alloys has shown that significant variations in alloy hardness can be obtained through modification of both alloy chemistry and subsequent heat treatment, which may be rationalised through considering the Gibbs energy and diffusion rates of the system [15].

In order to facilitate future alloy design and microstructural optimisation for alloy strength, further studies of the $L1_2$ precipitation behaviour of cupronickels, are required. However, it is considered advantageous for such studies to be initially performed on compositionally simpler alloys to avoid the complications that arise from multiple precipitating phases and the associated elemental partitioning. To this end, in this study, three cupronickel alloys with compositions of Cu– 5 at. % Al– x at. % Ni, where x = 5, 15, 25, were investigated. The temporal evolution of the microstructure and hardness of each alloy was evaluated following exposures at 700˚C for up to 1000 hours and rationalised by considering the dislocation interactions mechanisms expected of A1-$L1_2$ alloys. In addition, the discontinuously precipitated $L1_2$ colonies were studied and their occurrence related to grain boundary character.

## 2. Experimental Procedure

The compositions of the alloys studied, given in Table 1, were chosen to be in line with existing precipitation strengthened cupronickels. The positions of these alloys in the Ni-Cu rich region of the Al-Cu-Ni ternary phase diagram are shown in Figure 1. Alloys A, B and C were arc melted from pure elements of at least 99.9% purity and each ingot was inverted and remelted 5 times to reduce cast compositional inhomogeneities. All alloys were homogenised for 100 hours at a temperature ~ 50˚C below the experimentally obtained solidus temperatures, Table 1. Following homogenisation, sections from each ingot were aged at 700˚C for 1, 10, 100 and 1000 hours and air cooled. All heat treatments were performed in argon backfilled quartz ampoules to minimise environmental interactions.

Differential Scanning Calorimetry (DSC) was performed on disc-shaped specimens, measuring 5 mm in diameter by 1 mm thick, cut from the homogenised ingots. Calorimetric data were collected from the samples under an argon atmosphere using a Netzsch 404 instrument with a heating/cooling rate of $10^{\circ}Cmin^{-1}$. The results were analysed using the first deviation from baseline approach in order to obtain the solidus, liquidus and precipitate solvus temperatures. Samples for scanning electron microscopy (SEM) were prepared following standard metallographic preparation techniques, culminating in a final polishing stage using a $H_2O_2$ neutralised solution of 0.06 μm colloidal silica. In addition, where indicated, electrolytic etching using a 10% phosphoric acid solution at ~ 5 V was used to enhance the contrast and facilitate the analysis of the $L1_2$ particles. Two scanning electron microscopes were used: an FEI Nova NanoSEM 450 equipped with an e$^-$Flash1000 Electron Backscattered Diffraction (EBSD) detector and a Zeiss GeminiSEM 300 equipped with an Oxford Instruments Energy Dispersive X-ray Spectroscopy (EDX) detector. The actual compositions of the three alloys were determined in the as-homogenised state using SEM-EDX by averaging over at least 5 randomly selected large areas (500 $\mu m^2$).

*Table 1: Nominal and EDX-measured compositions of alloys A, B and C, in at. %, with solidus temperatures as determined by DSC and homogenization temperatures used.*

| **Alloy** | **Cu** | | **Ni** | | **Al** | | **Solidus (˚C)** | **Hom T. (˚C)** |
|---|---|---|---|---|---|---|---|---|
| | Nom. | EDX | Nom. | EDX | Nom. | EDX | | |
| **A** | 90 | 90.3 ± 0.4 | 5 | 4.6 ± 0.2 | 5 | 5.1 ± 0.4 | 1090 | 1040 |
| **B** | 80 | 78.5 ± 0.2 | 15 | 15.6 ± 0.2 | 5 | 5.9 ± 0.2 | 1125 | 1075 |
| **C** | 70 | 67.8 ± 0.2 | 25 | 25.9 ± 0.1 | 5 | 6.2 ± 0.1 | 1160 | 1110 |

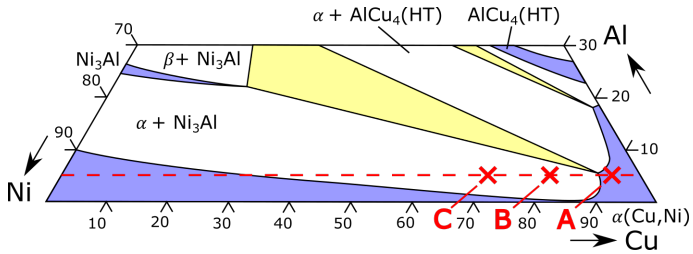


*Figure 1: A section of the Cu-Ni-Al ternary phase diagram at 700˚C, adapted from [8]. Alloy A lies in the A1 solid solution while Alloys B and C are shown to lie within the A1/L1$_2$ binary phase field.*

Analysis of the particle size distributions was performed using the ImageJ software on SEM images of a minimum of 350 particles. Overlapping particles were excluded from the data by both limiting the selection to circularities greater than 0.7 and manually evaluating the particles chosen. The average particle diameter was obtained following the procedure outlined by Goodfellow *et al*. [16]. Assuming a spherical morphology, the effective particle diameters were binned according to the Freedman Diaconis method [17] and were fitted with the lognormal distribution given in Eq. 1 using the Wavemetrics Igor Pro software package. The average precipitate size was taken as the median of the lognormal function ($e^{\mu}$) with upper and lower uncertainties given by the width of the function away from the median ($e^{(\mu+\sigma)}$ and $e^{(\mu-\sigma)}$), where $\sigma$ is the standard deviation associated with the median, $\mu$.

$$f(x) = \frac{1}{x\sigma\sqrt{2\pi}} \exp\left(-\left[\frac{(\ln(x)-\mu)^2}{2\sigma^2}\right]\right) \qquad \text{Equation 1}$$

X-ray Diffraction (XRD) data were acquired across the 2θ angular range from 20˚ to 100˚ on a Bruker D8 diffractometer using Ni-filtered Cu-Kα radiation. Diffraction patterns were fitted using the Pawley method [18] in the TOPAS-academic software package to obtain the lattice parameters of the precipitate, α–L1$_2$, and matrix, α–A1, phases. The lattice misfit ($\delta$) was calculated using Eq. 2.

$$\delta = 2\left[\frac{\alpha_{L1_2} - \alpha_{A1}}{\alpha_{L1_2} + \alpha_{A1}}\right] \qquad \text{Equation 2}$$

The hardness in each condition was determined using a Vickers hardness indenter with an applied load of 1, 2, 3 or 5 kg depending on the hardness of the sample, and a dwell time of 15 seconds. The indenter was calibrated each time the load was changed, and at least eight measurements were averaged to obtain a value of hardness and associated standard deviation for each sample condition.

# 3. Results

The actual compositions of the three alloys in the homogenised state are given in Table 1. All alloys were found to be within 1.5 at. % of the nominal target compositions and were therefore considered to be acceptable for the purposes of the study.

## 3.1 Differential Scanning Calorimetry

The DSC thermograms obtained during heating of Alloys A, B and C in their homogenised states are shown in Figure 2i. The thermogram from Alloy A displayed a single endothermic event between 1100 and 1200˚C, consistent with the bulk melting of the alloy. The absence of additional features at lower temperatures was consistent with the alloy retaining a single-phase microstructure throughout the DSC test. In contrast, the DSC thermograms from Alloys B and C showed a sigmoidal feature between 800 and 900˚C, consistent with a solid-state phase transformation, as well as an endothermic peak at temperatures over 1100˚C associated with bulk melting. This solid-state phase transformation in the 800 and 900˚C range is believed to be due to the dissolution of the L1$_2$ phase, which is expected to form on cooling from the homogenisation heat treatment. In Figure 2ii, the liquidus, solidus and L1$_2$ solvus temperatures obtained from the as-homogenised DSC thermograms are plotted as a function of the nominal Ni content in the alloy. Both the liquidus and solidus temperatures were found to increase with increasing Ni concentration in the material, whereas the L1$_2$ solvus temperature in Alloys B and C was found to remain constant at about 830˚C.

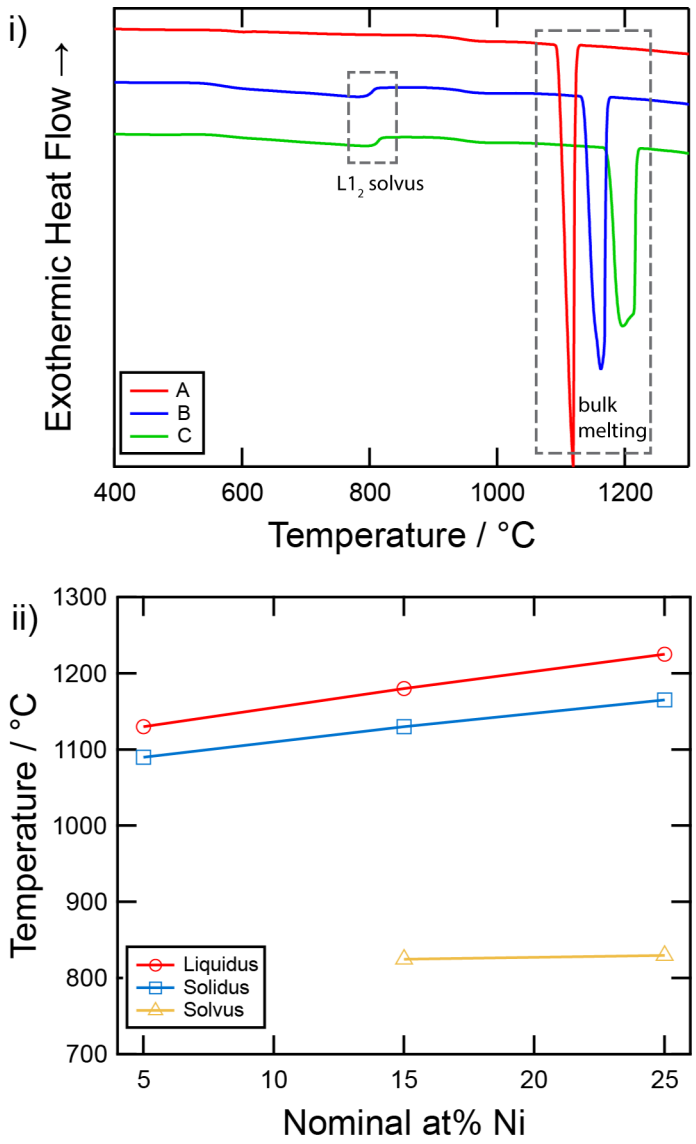


*Figure 2 i.) DSC thermograms obtained during heating of Alloys A, B and C in their as-homogenised states. ii.) Liquidus, solidus and $L1_2$ solvus temperatures obtained from the DSC results of the as-homogenised samples plotted as a function of nominal at. % Ni.*

## 3.2 Microstructural Evolution

### 3.2.1 Continuous Precipitation

Microstructural examination of Alloy A following each heat treatment confirmed that this alloy remained within a single fcc phase field at all conditions tested, consistent with its composition lying in the single phase field of the ternary phase diagram shown in Figure 1 and the absence of a deviation in the DSC results below the solidus temperature. Representative SEM images of the microstructures of the intragranular, continuous $L1_2$ precipitate distributions from Alloys B and C following exposures at 700˚C are shown in Figure 3.

In the microstructures obtained from the samples aged for 1 hour, continuous intragranular $L1_2$ precipitates were observed that were spheroidal and uniformly distributed. Following 10 and 100 hours at 700˚C, the morphology of the particles became progressively more cuboidal. In addition, the precipitates were observed to align along two orthogonal directions. After 1000 hours at 700˚C, the particles returned to a spherical morphology whilst maintaining their alignment, and some particles appeared conjoined along their alignment axes. The mean particle diameters calculated for Alloys B and C, as defined by the median of the lognormal distribution described above, are shown in Figure 4. Both alloys were found to exhibit remarkably similar coarsening behaviour, with particle diameters increasing progressively from ~ 30 nm to ~ 190 nm during ageing at 700˚C.

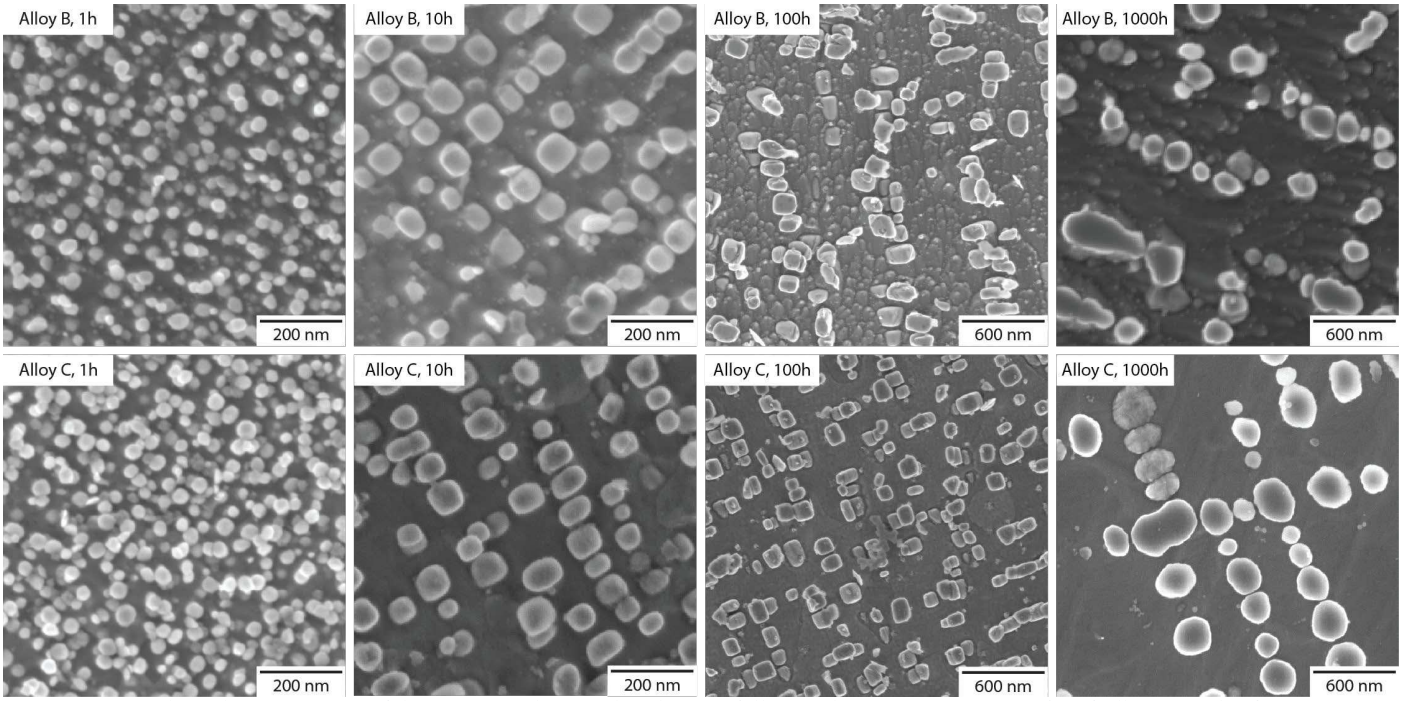


*Figure 3: Secondary electron images of the intragranular $L1_2$ distributions following heat treatments at 700˚C of Alloys B and C for 1, 10, 100 and 1000 hours.*

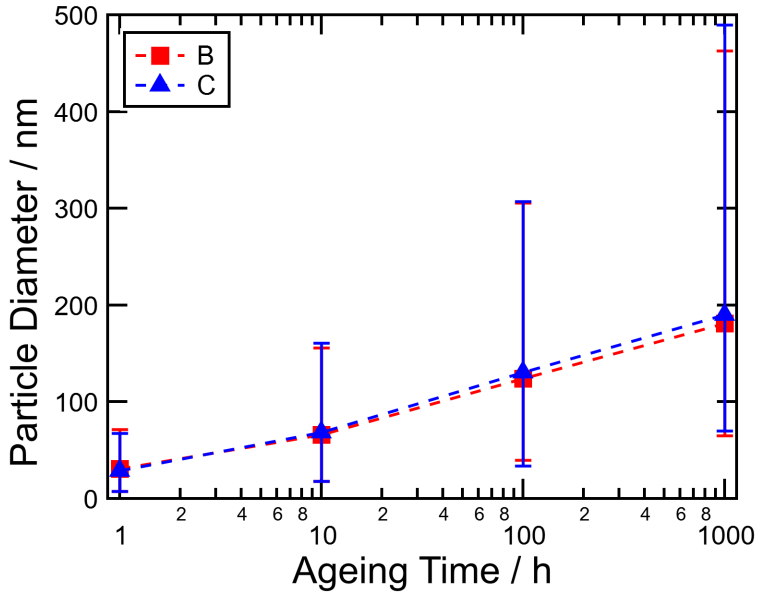


*Figure 4: Particle diameters of Alloys B and C after 1, 10, 100 and 1000-hour heat treatments at 700˚C.*

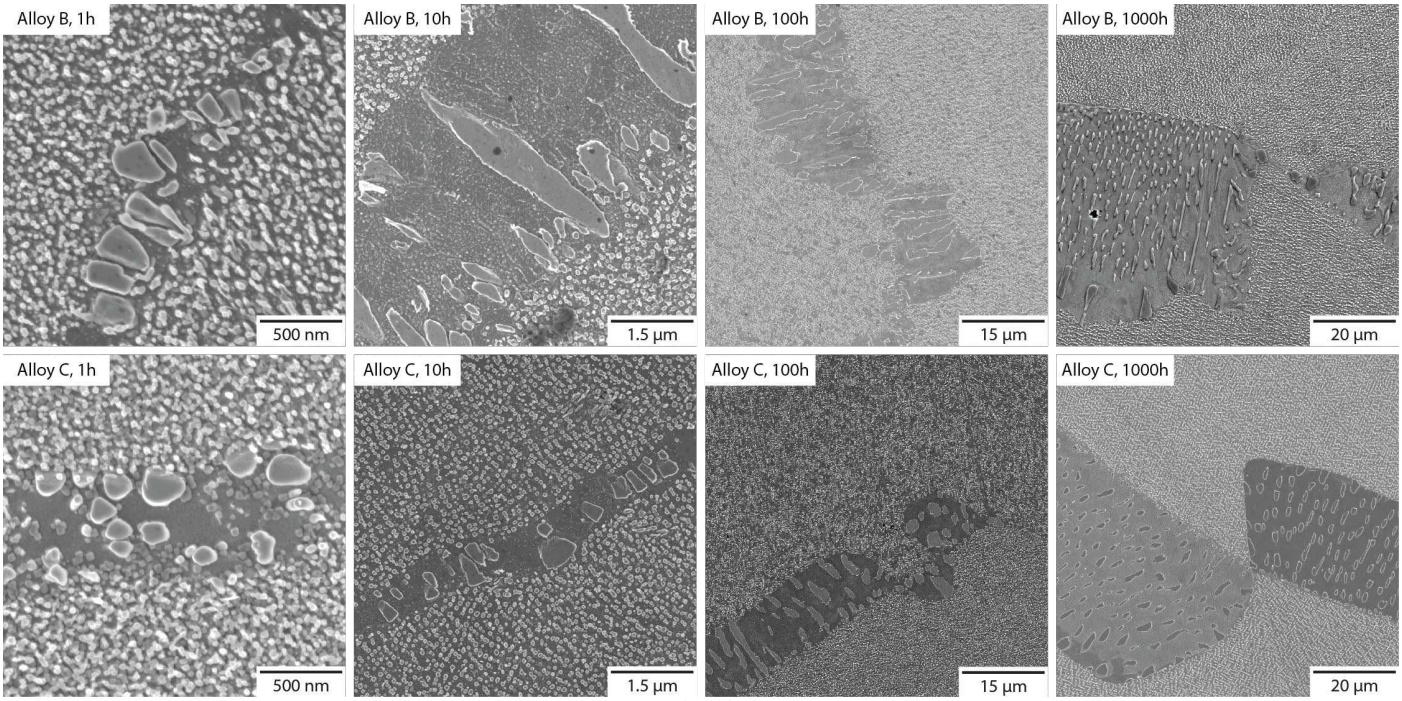

*Figure 5: Secondary electron images following heat treatments at 700˚C of Alloys B and C for 1, 10, 100 and 1000 hours, showing discontinuous precipitation colonies at grain boundaries.*

### 3.2.2 Discontinuous Precipitation

Discontinuous precipitation (DP) of the $L1_2$ phase was observed in both Alloys B and C for all ageing times, as shown in Fig. 5. In all cases, these DP colonies were located at grain boundaries and comprised a precipitate-free matrix in between discontinuously formed precipitate. The discontinuous products in both Alloys B and C were found to coarsen with time at temperature, whilst additional DP colonies were also observed in samples that were exposed for longer durations. The inter-particle spacing within the DP colonies, which is often used to determine the coarsening behaviour [19], was found to be irregular in most colonies and in some cases it was observed to be coarser with distance from the original boundary, e.g. Alloy B following 1000-hour exposure, Fig 5.

EDX elemental distribution maps of representative DP colonies in Alloys B and C after 1000 hours are shown in Figs. 6 and 7, respectively. Ni and Al were found to segregate to the discontinuously formed precipitates. Point EDX analyses of the phases indicated that the composition of the discontinuously precipitating phase in both Alloys B and C was very similar and in line with the composition of the $L1_2$ phase corresponding to $(Ni,Cu)_3Al$.

Discontinuous precipitation in Alloys B and C was found to evolve with exposure time, with “single-seam” morphologies being observed following short duration exposures of up to 10 hours, whereas both “single-seam” and “double-seam” morphologies were observed in the samples exposed for durations in excess of 100 hours [19].

EBSD analyses of the DP colonies were performed on samples of Alloys B and C after the 1000-hour exposures in order to identify the relationship between the discontinuous reaction products and the neighbouring grains, Fig. 8. This enabled unambiguous identification of the location of the resulting grain boundary and direction of the discontinuous reaction front. It was found that the discontinuous precipitation was prevalent at high angle grain boundaries, although not all high angle boundaries showed evidence of DP, Fig. 8ii. The DP colonies were observed to coarsen away from the original grain boundary, as seen in Figs. 8i and 8iii. Careful observation of the EBSD maps shown in Figs. 8ii and 8iv, also revealed large discontinuous $L1_2$ precipitates with orientations consistent with the DP colony forming ahead of the migrating boundary. Unusually, the formation of a discrete discontinuous colony was observed to form at the interface between a twin (depicted in orange) and a grain (pink) in Alloy C, Fig. 8iv. These analyses aid in interpreting the secondary electron images of the discontinuous reaction colonies presented in Fig. 5. For example, direct comparison can be made between the secondary electron image for Alloy C after 1000 hours shown in Fig. 5 and the backscattered electron image and EBSD map of the same region shown in Fig. 8iii and iv respectively. This enables the morphological features associated with the original grain boundaries and reaction fronts to be more readily identified.

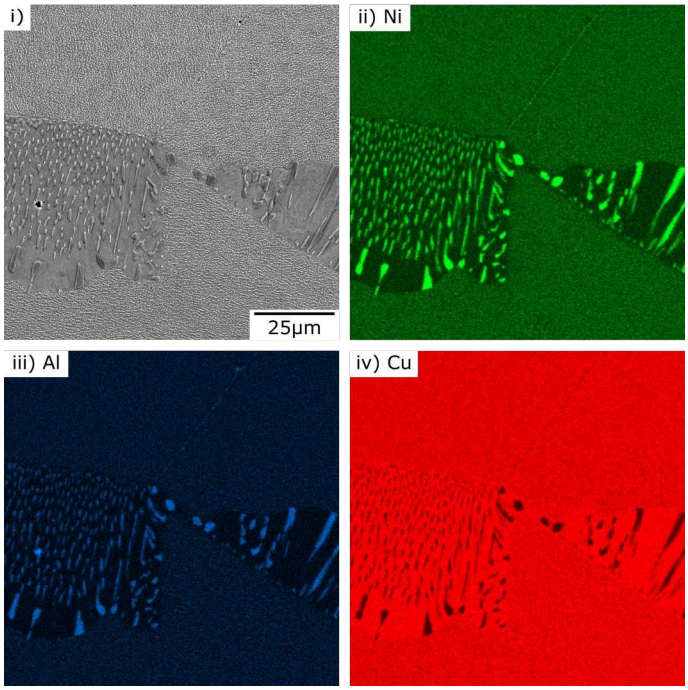


*Figure 6: Secondary electron image (i) and EDX elemental distribution maps (ii-iv) of discontinuously precipitated colonies at a triple grain boundary in Alloy B after a 1000-hour heat treatment at 700˚C.*

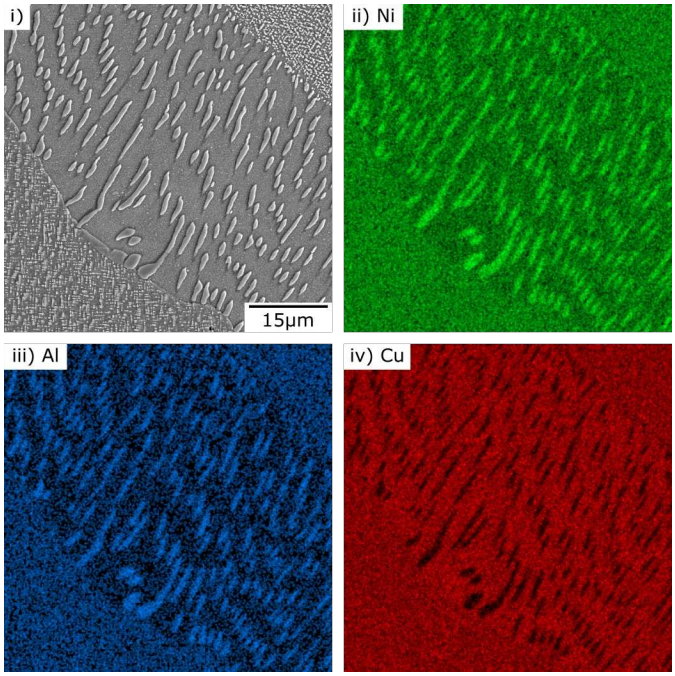


*Figure 7: Secondary electron image (i) and EDX elemental distribution maps (ii-iv) of a discontinuously precipitated colony in Alloy C after a 1000-hour heat treatment at 700˚C.*

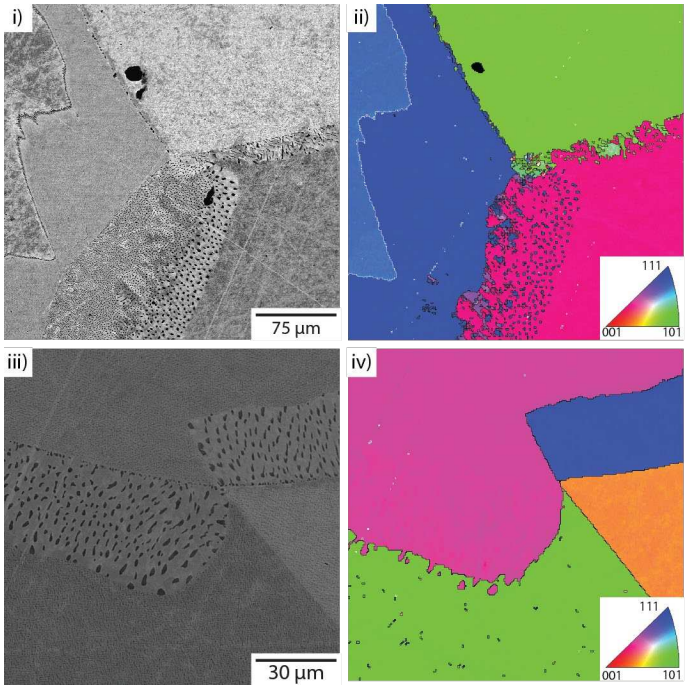


*Figure 8: Backscattered electron (left) and EBSD (right) images of Alloy B (i-ii) and Alloy C (iii-iv) after 1000 hours at 700˚C. Low angle grain boundaries (<15˚) are indicated in white, whereas high angle grain boundaries (>15˚) are shown in black. Discontinuous colonies can be seen in each image at high angle grain boundaries.*

## 3.3 X–ray Diffraction

The temporal evolution of the microstructure was also investigated using laboratory XRD of the samples in the as-homogenised state and following the ageing heat treatments. A subset of XRD data for Alloy B after 10-hour thermal exposure at 700˚C is shown in Fig. 9i, along with the associated fit using the Pawley method [18]. The lattice parameters of each phase obtained from the Pawley analysis are presented in Fig. 9ii and the lattice misfit between the A1 and $L1_2$ phases is shown in Fig. 9iii as a function of the logarithm of ageing time.

The lattice parameters of the A1 phase in all the alloys tested did not vary by more than 0.01 Å. Following thermal exposure, the A1 phase lattice parameter in Alloys B and C was found to decrease compared to that in the as-homogenised state, and did not show significant variation with varying ageing time. In addition, the $L1_2$ phase lattice parameter in Alloy C was found to remain approximately constant for the samples exposed up to 100 hours, whereas a pronounced decrease in the lattice parameter was observed for the sample exposed for 1000 hours. Whilst similar results were expected for Alloy B, a significant deviation was observed in the data obtained for the sample exposed for 100 hours. This is believed to be erroneous as the XRD patterns obtained from this sample were found to be textured, resulting in biased sampling of the material, and hence the data were not representative of the overall microstructure. However, as with Alloy C, Alloy B showed a marked decrease in the $L1_2$ phase lattice parameter for the sample exposed for 1000 hours.

The lattice misfit for Alloys B and C was calculated using Eq. 2 and was determined to be negative for all ageing times, Fig. 9iii. The lattice misfit behaviour of Alloys B and C was found to differ slightly as the lattice misfit for Alloy B was observed to generally decrease with increasing exposure time, whereas the lattice misfit in Alloy C was found to marginally increase up to an exposure time of 100 hours and then dramatically decrease in the 1000-hour sample.

## 3.4 Hardness

To investigate the effect of the microstructural changes on the strength of the material, hardness measurements were taken on all samples and the averaged results are presented in Fig. 10. The hardness of Alloy A in the as-homogenised state was 50 ± 1 Hv, and remained roughly constant for all ageing times, consistent with it having a single-phase solid solution microstructure without $L1_2$ precipitates. Alloys B and C showed hardness of 255 ± 7 Hv and 229 ± 4 Hv in the homogenised state, respectively. Both Alloys B and C showed a peak in hardness following the 1-hour exposure at 700˚C. After longer exposures at 700˚C, continual decreases in the hardness of the alloys were observed, which were found to decrease to values below that of the homogenised state following exposures of 10 hours or more.

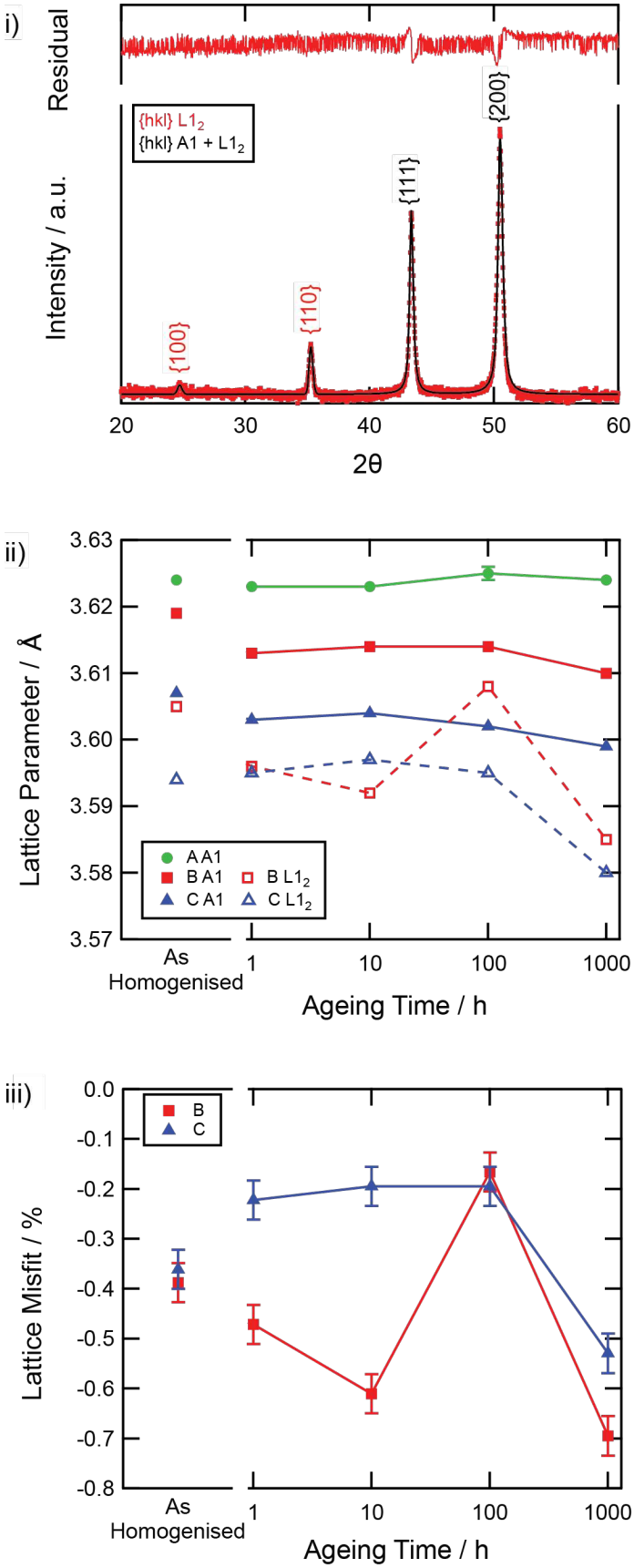


*Figure 9: i) Subset of an X-ray diffraction pattern obtained from Alloy B in the as-homogenised state overlaid with the associated fit computed using the Pawley method [18]. ii) Lattice parameters of the A1 and L1₂ phases in Alloys A, B and C as a function of ageing time at 700°C. iii) Lattice misfit between the A1 and the L1₂ phases for alloys B and C as a function of ageing time.*

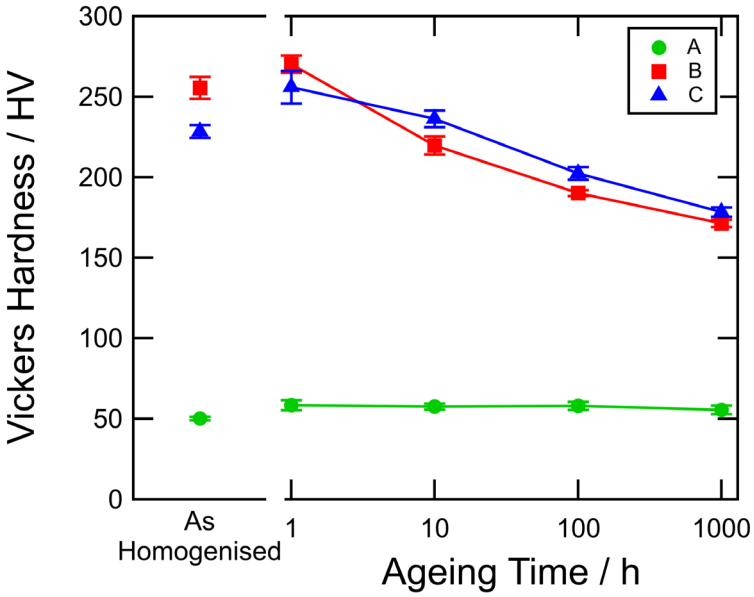


*Figure 10: Vickers hardness measurements as a function of ageing time for alloys A, B and C.*

# 4. Discussion

## 4.1 Continuous Precipitation

Alloys B and C, which contained 15 and 25 at. % Ni respectively, showed precipitation of the $L1_2$ phase, consistent with the ternary phase diagram shown in Fig. 1. Whilst the $L1_2$ phase was only visually identified during SEM imaging of the samples aged at 700˚C, the results from both the DSC and XRD indicated that the $L1_2$ phase was also present in the as-homogenised samples. This is attributed to the formation of the $L1_2$ phase on cooling from the homogenisation temperature, producing precipitates too fine to be imaged by SEM. A particular aim of this study was to investigate the temporal evolution of the $L1_2$ phase. In order to induce sufficient change over short time periods, 700˚C was selected as the ageing temperature as it is sufficiently near the $L1_2$ precipitate dissolution temperature as to ensure quick microstructural changes, but not so close to the $L1_2$ solvus temperature so as to result in incipient melting.

Exposures of varying durations at 700˚C resulted in both coarsening and morphological changes of the $L1_2$ precipitates in Alloys B and C. The morphology of the precipitates was found to transition from spherical to cuboidal, whilst the particles were found to align with the elastically soft <100> axes of the matrix following the 1000-hour exposures, consistent with the results of Stobrawa *et al.* [20]. The morphological evolution of the $L1_2$ phase was also found to be largely in agreement with existing theories applied to A1-$L1_2$ microstructural evolution in Ni-based superalloys [21, 22, 23]. However, no apparent correlation was observed between the morphologies of the $L1_2$ particles and the lattice misfit shown in Fig. 9, as Alloys B and C were found to exhibit near identical morphological changes, whereas the lattice misfit evolution of the two alloys was found to be markedly different. The magnitude of the lattice misfit in Alloy B was found to increase with increasing ageing time. In contrast, the magnitude of the lattice misfit in Alloy C was found to remain approximately constant for ageing times up to 100 hours, and increase dramatically in the sample exposed for 1000 hours. This disparity in the behaviour of the two alloys would suggest that the lattice misfit, and hence the interfacial strain energy between the A1 and $L1_2$ phases, is not the dominant mechanism in the morphological evolution of the precipitates. Furthermore, the strong alignment of the particles following the 1000-hour ageing, as well as the coalescence of the particles along the elastically compliant crystallographic axes would suggest that a loss of coherency occurred, as is known to occur during rafting in superalloys [24].

In addition to the morphological changes, appreciable coarsening of the $L1_2$ precipitates was observed in Alloys B and C, with the precipitate diameters increasing approximately linearly with ageing time. In both alloys the precipitates increased from about 30 nm after 1 hour at 700˚C to 180 nm (Alloy B) and 190 nm (Alloy C) after 1000 hours. This linear coarsening behaviour is inconsistent with the diffusion controlled precipitate growth described by the Lifshitz, Slyozov and Wagner (LSW) theory [25], suggesting that other factors are influencing precipitate growth kinetics. One possibility, particularly in the shorter time periods investigated, is that nucleation of new particles may be occurring

such that this time period is not exclusively within the growth regime. Alternatively, this could also be a result of particle agglomeration, which restricts the extent to which a particle can grow. This effect has also been seen in γ′ coarsening within polycrystalline Ni-based superalloys after 2000 hours at 850 ˚C [26, 27]. Indeed, evidence of particle alignment and coalescence can be readily seen in Fig. 3, most clearly in the microstructures of Alloys B and C after 1000 hours.

The microstructural changes observed had a profound effect on the measured hardness of the samples. Alloys B and C showed significantly higher hardness than Alloy A for all ageing times, consistent with the hardening effect of the $L1_2$ precipitates. Peak hardness was achieved for Alloys B and C after 1 hour at 700˚C, after which monotonic softening was observed for longer ageing times. In order-strengthened alloys, where the precipitates exhibit chemical ordering and are often a superstructure of the parent matrix, further energy barriers are introduced associated with the disruption of the ordered structure. For A1-$L1_2$ systems, the creation of an anti-phase boundary (APB) is observed when dislocations from the A1 phase transition into the $L1_2$ precipitates. To minimise the APB energy, deformation occurs by the passage of pairs of superpartial dislocations, and maximum hardness is achieved by the transition from weakly coupled to strongly coupled superpartial dislocations [28, 29, 30, 31].

Eqs. 3 and 4, which describe the change in critical resolved shear stress for weak and strong coupling were used to determine the optimum particle size $d^*$, as derived by Kozar *et al.* [32] and Brown and Ham [33], respectively:

$$\Delta\tau = \frac{1}{2}\left(\frac{\gamma_{APB}}{b}\right)^{\frac{3}{2}}\left(\frac{b\,d^*f}{T}\right)^{\frac{1}{2}}A - \frac{1}{2}\left(\frac{\gamma_{APB}}{b}\right)f \qquad \text{Equation 3}$$

$$\Delta\tau = \frac{1}{2}\left(\frac{Gb}{d^*}\right)f^{\frac{1}{2}}A\,w\left(\frac{\pi\,d^*\gamma_{APB}}{wGb^2} - 1\right)^{\frac{1}{2}} \qquad \text{Equation 4}$$

In each equation: $\gamma_{APB}$ is the APB energy of the $L1_2$ phase; $b$ is the Burger's vector; $d^*$ is the critical particle size; $f$ is the volume fraction of particles; $T$ is the line tension, taken to be equal to $Gb^2/2$ for screw dislocations; $A$ is a geometrical factor equal to 0.72 for spherical precipitates; $G$ is the shear modulus of the material and $w$ is a dislocation repulsion factor approximated to 1 following Hüther *et al*. [34]. The $\gamma_{APB}$ was calculated using the Miodownik and Saunders approach [35, 36] and the ThermoCalc software package coupled with the TTNi8 database. The APB energies for Alloys B and C were thus found to be 278.6 and 217.6 $mJm^{-2}$ respectively, by taking the average APB along {111} and {001}. The Burger's vector was assumed to be of the a/2[110] type, with a being the lattice parameter of the A1 matrix and assigned a value of 3.6 Å on average. The shear modulus of the material was calculated to be 45 GPa, obtained using the elastic modulus E of a Cu-6.2Ni-6.8Al at% alloy [37] and assuming the material is isotropic. The elastic and shear moduli of the commercially produced Cu-Ni-Al alloys, Hiduron® 130 and Hiduron® 191, support the assumption of isotropy, and the shear modulus used in these calculations is 85% that of the Hiduron® alloys, as expected for model alloys. Due to limitations with sample preparation, the volume fraction of precipitates could not be reliably determined, and hence, a range of optimum particle sizes were calculated by varying the volume fraction from 0.1 to 0.5. The optimum sizes were found to range from 16 to 23 nm and 20 to 29 nm for Alloys B and C, respectively. It is important to note that many of the values used in these equations are temperature dependent and, therefore, the optimum particle diameters will also exhibit a temperature dependency. However, it is expected that the range in particle diameters obtained by varying the precipitate volume fractions results in a wider distribution and therefore, encompasses the temperature dependency.

Experimentally, the greatest hardness was obtained after ageing both Alloys B and C for 1 hour at 700˚C and in this condition the mean particle sizes for both alloys were ~30 nm. This places the hardening mechanism in the strongly coupled regime for both alloys, and relatively near the calculated critical precipitate size for maximum hardness. Given that the $L1_2$ phase was not visible in the homogenised samples using SEM and the lower hardness measured from samples in this condition with respect to the 1 hour heat treatment, the homogenised condition samples are expected to operate in the weakly coupled regime. These results have important implications for the design of post-processing heat treatments in order to optimise the mechanical properties of the alloys. From the precipitate sizes measured in this study, along with the mid-point optimum precipitate sizes calculated using the transition from weakly to strongly coupled dislocations, an optimum heat treatment duration of between 30 mins and 1 hour at 700˚C for Alloys B and C respectively is predicted. This approach could be extended to heat treatment optimisation at other temperatures, where changes in the Gibbs energy driving forces and diffusion rates have been shown to generate different particle size distributions and resulting alloy hardness [15].

## 4.2 Discontinuous Precipitation

In addition to the continuous precipitation of the $L1_2$ phase, DP was also observed at the grain boundaries in Alloys B and C, Fig. 5. The DP process is well documented in Cu alloys [38, 19], and has been studied in the Cu-Ni-Al system [12, 11, 39, 40]. It is known that it occurs in a supersaturated solid solution in which continuous precipitation is kinetically inhibited [19]. High angle grain boundaries act as fast paths for the diffusion of solute atoms, allowing DP to occur through grain boundary migration; grain boundary curvature provides a driving force for grain boundary migration, and a second phase is discontinuously precipitated with a regular spacing as solute accumulates at the interface. This results in the supersaturated matrix decomposing into lamellar (or rod-like) aggregates in a eutectoid-like decomposition. As the parent and product phases are the same, this process conforms to a type II discontinuous reaction as defined by Williams and Butler [41] and discussed in the works of Manna *et al.* [38,19].

The driving force for DP in the samples studied may be due to the limited solubility of Al in (Cu-Ni), which was found to be 0.1 to 0.8 at. % Al in Cu solutions containing 10 to 20 at. % Ni [42]. This is supported by the work of Sierpinski *et al.* [39], who showed limited DP in Cu-Ni-Al alloys cooled slowly from 900˚C to 500˚C. Slow cooling allowed for the solute redistribution required for continuous precipitation. Coarser precipitates were also seen at longer ageing times, which is consistent with a diffusion-controlled process.

Many isothermal steady state models exist for the analysis of DP [19]. All, however, depend on either the lamellar spacing or the angle between the lamellae and the normal to the reaction front. Determination of either parameter was not possible in this case due to the morphology and alignment of the DP products with the normal to the migrating boundary. Multiple possible explanations exist for the apparently particulate nature of the DP. Reprecipitation at the migrating boundary is known to occur as an alternative to branching to maintain a constant lamellar spacing. Alternatively, rod-like DP has been previously reported, and would appear ellipsoidal if the plane of observation does not intersect the rods along the long axis. Sierpinksi *et al.* [39] observed rod-like DP in Cu-10Ni-3Al (wt%) alloys after isothermally ageing at 500˚C following a water-quench from 900˚C. Furthermore, at high temperatures increased diffusion can result in a considerable proportion of continuous coarsening rendering the DP colony completely spheroidised [19]. Given the relatively high homologous temperature the latter mechanism may be in operation in the alloys investigated in this study. Spheroidal DP has also been previously reported in Hiduron® 130 for samples aged at 600 and 700˚C for 100 hours [12], on which the model Cu-Ni-Al alloys studied are based.

Many of the DP colonies in Alloys B and C coarsened with time, or equivalently, with distance from the original grain boundary. It has been reported by Manna *et al.* [38, 43, 19] that the presence of prior or concurrent continuous precipitation ahead of the reaction front dramatically reduces the chemical driving force for DP. Furthermore, continuous precipitation may act as a physical obstacle to the motion of the boundary. The relative importance of each effect is not known, but they may lead to a reduction in the reaction front migration rate. The slower reaction front provides a longer time for the diffusion of solute, causing an increase in lamellar spacing in the latter stages compared to that of the early stages of the same transformation. This phenomenon has been seen in a number of alloy systems, including Cu-Mg [44] and Cu-Sn [45].

The occurrence of the double-seam morphology observed in Fig. 5 is not well understood, and indeed two theories will be discussed based on two proposed mechanisms for the initiation of DP. The first is based on the pucker mechanism, which relies on a rigid orientation relationship between the precipitate and matrix. Nucleation of allotriomorphs on stationary boundaries leads to boundary deflection, which is necessary to minimise interfacial energy and maintain the rigid precipiate/matrix habit plane. Based on this mechanism, the double-seam morphology is predicted to occur in the temperature range $T > 0.5T_s$ where $T_s$ is the solidus temperature [19, 46]. This is due to the boundary sensitivity to structure and hence, it's restriction at low temperatures. However, there is also evidence for the formation of a double-seam at $T > 0.5T_s$ [47], and as a consequence it has been suggested that the double-seam morphology could nucleate via a thermally activated boundary migration process.

The DSC data acquired in this study indicated that the solidus temperatures of Alloys B and C were 1130 and 1165˚C, respectively. At 700˚C, this places the ageing temperature firmly > 0.65 $T_s$, providing evidence contrary to the pucker mechanism in Cu-Ni-Al alloys. Indeed, the rough surfaces of the discontinuous precipitates and their alignment perpendicular to the migrating boundary do not support the idea of a strong habit relationship, despite the crystallographic alignment of the continuous precipitates at intermediate ageing times. Therefore, this provides further evidence for thermally activated boundary migration as the initiation mechanism, and also suggests the double-seam

morphology depends on local thermodynamics and kinetic considerations, including grain boundary structure and mobility [19].

EBSD confirmed that DP occurred at high angle grain boundaries, but the grains were too large to allow statistical analysis. In addition, whilst it is commonly expected that discontinuous reactions occur at mobile high angle boundaries [19], DP has also been observed to occur at a twin interface in Cu-Mg alloys [48]. Hence, additional work on the occurrence of DP and under what conditions this may happen is required.

EBSD data shown in Fig. 8iv revealed that discontinuously precipitated particles were observed ahead of the reaction front to which they belonged. The particle orientation matched that of the neighbouring grain, and they appeared to reside as incoherent particles in a precipitate free matrix. It therefore appears that the discontinuous reaction front is led by growth of $L1_2$ tendrils from the initiating boundary, which relieve the supersaturation in the neighbouring grain. This is followed by matrix reorientation, which lags behind the $L1_2$ formation. Such a hypothesis is consistent with the findings of Dong *et al*. [15]. However, higher resolution compositional and crystallographic analysis would be required to fully characterise the mechanism by which this process occurs.

# 5.Conclusion

The microstructure of three $Cu_{(95-x)}Ni_xAl_5$ alloys containing 5, 15 and 25 at. % Ni were characterised using a combination of SEM, EDX, EBSD and XRD techniques, in the homogenised condition and following 1, 10, 100 and 1000-hour heat treatments at 700˚C. From the results obtained the following conclusions were drawn:

- The formation of sub-micron continuously precipitated $L1_2$ particles was observed within the A1 matrix of alloys containing in excess of 15 at. % Ni.
- The coarsening behaviours of the continuous precipitates in Alloys B (15 at. %Ni) and C (25 at. % Ni) were remarkably similar, with both alloys exhibiting an initial particle size of ~30 nm following 1 hour exposures at 700˚C. These particles coarsened to 180 and 190 nm in Alloys B and C respectively following 1000 hours at 700˚C.
- The optimal particle sizes for maximum strengthening were calculated to be in the range of 16-29 nm for both Alloys B and C depending on the precipitate volume fractions. This could be achieved with a heat-treatment in the range of 30-60 minutes at 700˚C.
- Discontinuous precipitation of the $L1_2$ phase was observed at some high angle grain boundaries in Alloys B and C. These discontinuously precipitated colonies appeared to be led by the directional growth of $L1_2$ particles from the boundary. The matrix reorientation associated with this process lagged behind, leading to incoherent tendrils of the $L1_2$ phase extending into the neighbouring grain.


# Acknowledgements

The authors would like to acknowledge Sue Rhodes for experimental assistance. The original research data is available through doi: 10.15131/shef.data.12752705.


# Declaration of Interest

None

# Bibliography


1. C. D. S. Tuck, Z. Xianhua, D. E. J. Talbot, Hydrogen Embrittlement Of Ultrahigh Strength Cupronickel Alloy: Effects Of Exposure To Gaseous Hydrogen Environment On Fatigue Resistance, Br. Corros. J. 29 (1) (1994) 70–74. doi:10.1179/000705994798268051.

2. C. Tuck, The Development of Very High Strength Copper Alloys with Resistance to Hydrogen Embrittlement and Stress Corrosion Cracking (Jan 2005). URL https://www.onepetro.org/conference-paper/NACE-05462
3. Langley Alloys, Hiduron® Alloy 191: High strength cupronickel for marine service, Tech. rep., Langley Alloys Ltd.
URL https://www.langleyalloys.com/en/products/hiduron-191/
4. Langley Alloys, HIDURON 130: A very high strength cupronickel, Tech. rep., Langley Alloys Ltd (2008).
URL http://www.offshore-europe.co.uk/ novadocuments/92928?v=635725487239900000
5. M. S. Parvizi, A. Aladjem, J. E. Castle, Behaviour of 9010 cupronickel in sea water, Int. Mater. Rev. 33 (1) (1988) 169–200. doi:10.1179/imr.1988.33.1.169.
6. The Copper Development Association and The Nickel Development Institute, Copper- nickel alloys, properties and applications (1982). URL
https://www.copper.org/applications/marine/cuni/properties/DKI_booklet.html
7. R. W. Ross, Alloys for Marine Fasteners (2000).
URL https://www.nickelinstitute.org/ /media/Files/TechnicalLiterature/20130902-14054 ALLOYS FOR MARINE FASTENERS.ashx
8. P. Villars, A. Prince, H. Okamoto, Handbook of Ternary Alloy Phase Diagrams, Vol. 3, ASM International, 1995.
9. C. T. Sims, N. S. Stoloff, W. C. Hagel (Eds.), Superalloys II, John Wiley & Sons, Inc., New York, 1987.
10. ngley Alloys, Hiduron® 191 Datasheet (2017). URL https://www.langleyalloys.com/en/products/hiduron-191/
11. R. J. Grylls, C. D. S. Tuck, M. H. Loretto, Identification of Orthorhombic Phase in a High-Strength Curponickel, Scr. Mater. 34 (1) (1996) 121–126. doi: 10.1016/1359-6462(95)00490-4.
12. K. Christofidou, J. Robinson, P. Mignanelli, E. Pickering, N. Jones, H. Stone, The effect of heat treatment on precipitation in the Cu-Ni-Al alloy Hiduron® 130, Mater. Sci. Eng. A 692 (March) (2017) 192–198. doi:10.1016/j.msea.2017.03.069.
13. R. J. Grylls, C. D. Tuck, M. H. Loretto, Strengthening of a cupronickel alloy by an ordered $L1_2$ phase, Intermetallics 4 (7) (1996) 567–570. doi:10.1016/0966-9795(96)00050-7.
14. R. J. Grylls, Mechanical properties of a high-strength cupronickel alloy-Bayesian neural network analysis, Mater. Sci. Eng. 234-236 (1997) 267–270. doi: 10.1016/S0921-5093(97)00174-3.
15. B. W. Dong, J. C. Jie, S. H. Wang, Z. Z. Dong, W. T. M., T. J. Li, Novel insight into precipitation behavior of $\gamma'$ phase particles in Cu-15Ni-xAl alloys through Calphad method, Intermetallics 120 (2020) 106749. doi: 10.1016/j.intermet.2020.106749
16. A. J. Goodfellow, E. I. Galindo-Nava, K. A. Christofidou, N. G. Jones, T. Martin, P. A. Bagot, C. D. Boyer, M. C. Hardy, H. J. Stone, Gamma Prime Precipitate Evolution During Aging of a Model Nickel-Based Superalloy, Metall. Mater. Trans. A Phys. Metall. Mater. Sci. 49 (3) (2018) 718–728. doi:10.1007/s11661-017-4336-y.
17. D. Freedman, P. Diaconis, On the Histogram as a Density Estimator: L2 Theory, Probab. Theory Relat. Fields 57 (4) (1981) 453–476. doi: 10.1007/BF01025868.
18. G. S. Pawley, Unit-cell refinement from powder diffraction scans, J. Appl. Crystallogr. 14 (6) (1981) 357–361. doi:10.1107/S0021889881009618.
19. I. Manna, S. Pabi, W. Gust, Discontinuous reactions in solids, Int. Mater. Rev. 46 (2) (2001) 53–91. doi:10.1179/095066001101528402.
20. J. P. Stobrawa, Z. M. Rdzawski, Precipitation process of the $Ni_3Al$ phase in copper- based alloys, J. Achiev. Mater. Manuf. Eng. 15 (1-2) (2006) 21–26.
21. R. A. Ricks, A. J. Porter, R. C. Ecob, The Growth of $\gamma'$ Precipitates in Ni-base Superalloys, Acta Metall. 31 (1983) 43–53. doi:10.1016/0001-6160(83)90062-7.
22. A. J. Ardell, The effects of elastic interactions on precipitate microstructural evolution in elastically inhomogeneous nickel-base alloys, Philospohical Mag. 94 (19) (2014) 2101–2130. doi:10.1080/14786435.2014.906756.
23. A. J. Ardell, The Growth of Gamma Prime Precipitates in Aged Ni-Ti Alloys, Metall. Trans. 1 (1970) 525-534.
24. F. R. N. Nabarro, Rafting in Superalloys, MMTA 27 (1996) 513530.
25. I. M. Lifshitz, V. V. Slyozov, The kinetics of preciptiation from supersaturated solid solutions, J. Phys. Chem. Solids 19 (1961) 35–50.
26. J. Safari, S. Nategh, M. Mclean, Evolution of microstructure of nickel base superalloy at high temperatures, Mater. Sci. Technol. 22 (8) (2006) 888–898. doi:10.1179/174328406X91168

27. D. Hadjiapostolidou, B. a. Shollock, Long Term Coarsening in René 80 Ni-base Superalloy, Superalloys 2008 11th Int. Symp. Superalloys (2) (2008) 733–739. URL http://www.tms.org/superalloys/10.7449/2008/Superalloys 2008 733 739.pdf
28. A. J. Ardell, Precipitation hardening, Metall. Trans. A 16 (12) (1985) 2131–2165. doi:10.1007/BF02670416.
29. D. P. Pope, S. S. Ezz, Mechanical properties of $Ni_3Al$ and nickel-base alloys with high volume fraction of γ', Int. Met. Rev. 29 (3) (1984) 136–167. doi: 10.1179/imtr.1984.29.1.136.
30. B. Reppich, Some New Hardening Aspects Concerning Particle Mechanisms in $\gamma'$ Precipitating Ni-base Alloys - I. Theoretical Concept, Acta Metall. 30 (1982) 87–94. doi: 10.1016/0001-6160(82)90048-7.
31. B. Reppich, P. Schepp, G. Wehnert, Some New Hardening Aspects Concerning Particle Mechanisms in $\gamma'$ Precipitating Ni-base Alloys - II. Experiments, Acta Metall. 30 (1982) 95–104. doi: 10.1016/0001-6160(82)90049-9.
32. R. W. Kozar, A. Suzuki, W. W. Milligan, J. J. Schirra, M. F. Savage, T. M. Pollock, Strengthening mechanisms in polycrystalline multimodal nickel-base superalloys, Metall. Mater. Trans. A Phys. Metall. Mater. Sci. 40 (7) (2009) 1588–1603. doi:10.1007/s11661-009-9858-5.
33. L.M. Brown and R.K. Ham, Strengthening Mechanisms in Crystals, Elsevier Publishing Company Ltd, London, 1971.
34. W. Hüther, B. Reppich, Order Hardening of MgO by Large Precipitated Volume Fractions of Spinel Particles, Mater. Sci. Eng. 39 (1979) 247–259. doi: 10.1016/0025-5416(79)90063-6.
35. A. Miodownik, N. Saunders, The calculation of APB Energies in $L1_2$ Compounds Using a Thermodynamic Database, in: P. Nash, B. Sundman (Eds.), Appl. Thermodyn. Synth. Process. Mater., 1995, pp. 1–14.
36. N. Saunders, M. Fahrmann, C. J. Small, The Application of CALPHAD Calculations to Ni-based Superalloys, Superalloys. Superalloys 2000 (2000) 803.
37. A. Rittapai, S. Urapepon, J. Kajornchaiyakul, C. Harniratisai, Properties of experimental copper-aluminium-nickel alloys for dental post-and-core applications, J. Adv. Prosthodont. J Adv Prosthodont 2156 (2014) 215–23. doi:10.4047/jap.2014.6.3.215.
38. I. Manna, S. K. Pabi, W. Gust, Discontinuous Precipitation in a Cu-12 at.% In Alloy, Acta Met. Mater. 39 (7) (1991) 1489–1496.
39. Z. S. Sierpin´ski, J. Gryziecki, Phase transformations and strengthening during ageing of CuNi10Al3 alloy, Mater. Sci. Eng. A 264 (1-2) (1999) 279–285. doi:10.1016/S0921- 5093(98)01083-1.
40. H. Tsuda, T. Ito, Y. Nakayama, The Improvement of Microstructures and Mechanical Properties in Cu-Ni-Al Alloys by Two-Step Ageing, Scr. Metall. 20 (1986) 1555–1559. doi: 10.1016/0036-9748(86)90394-7.
41. Williams, D. B. and E. P. Butler (1981). "Grain boundary discontinuous precipitation reactions." International Metals Reviews **3**: 153-183.
42. A. Prince, K. Kumar, Aluminium-Copper-Nickel, Ternary Alloy. 4 (1991) 597–629.
43. I. Manna, Grain Boundary Migration in Solid State Discontinuous Reactions, Interface Sci. 6 (1998) 113–131.
44. H. Tsubakino, R. Nozato, Discontinuous precipitation in Cu-Mg alloys, J. Mater. Sci. 19 (1984) 3013–3020.
45. H. Tsubakino, Discontinuous Precipitation in a Cu-Sn Alloy, Metallography 17 (1984) 371–382. doi: 10.1016/0026-0800(84)90074-0.
46. K. N. Tu, D. Turnbull, Morphology of Cellular Precipitation of Tin from Lead-Tin Bicrystals, Acta Metall. 15 (1967) 369–376. doi: 10.1016/0001- 6160(67)90214-3.
47. R. A. Fournelle, J. B. Clark, The Genesis of the Cellular Precipitation Reaction, Metall. Trans. 3 (1972) 2757–2767.
48. I. Manna, S. K. Pabi, W. Gust, Initiation sites for discontinuous precipitation in some Cu-base alloys, J. Mater. Sci. 26 (1991) 4888–4892.